




Scanning two-grating free electron Mach-Zehnder interferometer

Cameron W. Johnson ^{*,†}, Amy E. Turner,^{*} and Benjamin J. McMorran 

Department of Physics, University of Oregon, Eugene, Oregon 97403, USA

 (Received 21 April 2021; revised 3 September 2021; accepted 14 September 2021; published 4 October 2021)

We demonstrate a two-grating free electron Mach-Zehnder interferometer constructed in a transmission electron microscope. A symmetric binary phase grating and a condenser lens system form two spatially separated, focused probes at the sample which can be scanned while maintaining alignment. The two paths interfere at a second grating, creating constructive or destructive interference in the output beams. This interferometer has many notable features: positionable probe beams, large path separations relative to beam width, continuously tunable relative phase between paths, and real-time phase information. Here we use the electron interferometer to measure the relative phase shifts imparted to the electron probes by electrostatic potentials as well as a demonstration of quantitative nanoscale phase imaging of a polystyrene latex nanoparticle.

DOI: [10.1103/PhysRevResearch.3.043009](https://doi.org/10.1103/PhysRevResearch.3.043009)

I. INTRODUCTION

Electron holography and interferometry can enable nanoscale phase imaging [1,2], the exploration of the Aharonov-Bohm effect [3,4], interaction-free measurements and quantum electron microscopy [5–7], the measurement of coherence properties [8–10], quantum state tomography [11,12], and the coherent control of the free electron wave function [13]. While interferometry is widely used in optics and photonics fields such as astronomy [14], optical metrology [15], and quantum optics [16], electron interferometry has advanced at a slower pace, partially due to a lack of basic optical elements such as beamsplitters and mirrors that can be used to build a versatile system. Here we use two diffraction gratings as beamsplitters in a conventional transmission electron microscope (TEM) to create a flexible, path-separated Mach-Zehnder interferometer for free electrons, emulating the canonical example for phase sensitive interferometry.

Electron interferometers are currently limited and defined by the electron optical elements used to construct the interferometer. Electrostatic mirrors for free electrons show great promise, but are in their early development [17–19]. Beamsplitters have existed for decades, the most prevalent being electrostatic biprisms [20] which divide wavefronts. Biprisms generate interferograms from which the phase of the sample can be extracted after image processing. However, they require high spatial coherence [21]; thus, they are inherently limited by modern electron emission sources that are only partially coherent. Using recently improved diffraction grat-

ings as amplitude dividing beamsplitters [22–24] to create spatially separated paths evades the high spatial coherence requirement, if the separated paths are perfectly overlapped after the sample [25]. We note that amplitude division with microwave chip beamsplitters has also been demonstrated, but is not yet practical for electrons with kinetic energies above 200 eV [26].

Various demonstrations of matterwave interferometry have proceeded for decades [27]. Path-separated Mach-Zehnder interferometers specifically have been demonstrated for different kinds of matter waves, including neutrons [28], atoms [29], BECs [30], conduction and quantum Hall valley electrons in 2D devices [31,32], and SQUIDS [33]. Free electron Mach-Zehnder interferometers with discrete outputs have predominantly been constructed using nanofabricated diffraction gratings or crystals as beamsplitters. Two-plane electron interferometers fabricated from monolithic uniform crystals [34,35] and three-plane Mach-Zehnder interferometers with discrete crystal planes [27,36] have been demonstrated. A three-grating Mach-Zehnder interferometer for free electrons was demonstrated with nanofabricated transmission amplitude gratings [37]. These free electron interferometer variants have advanced electron interferometry and could potentially be used for imaging applications, but the compact longitudinal designs significantly restrict the types of experiments that can be performed.

Here we demonstrate a two-grating electron Mach-Zehnder interferometer (2GeMZI) constructed inside a conventional TEM that provides clearly defined isolated probes, arbitrary probe phase shifts, and scanning/imaging capabilities. Furthermore, since this is a scanning probe technique, the magnification can be changed without adjusting the setup, unlike electron holography. This is accomplished by placing diffraction gratings in apertures above and below the specimen plane of a TEM operated in scanning TEM (STEM) mode. The small deviations of the lens and aperture positions from the nominal STEM settings allow us to maintain the high resolution imaging capabilities afforded by the TEM

^{*}These two authors contributed equally to this work.

[†]cwj@uoregon.edu

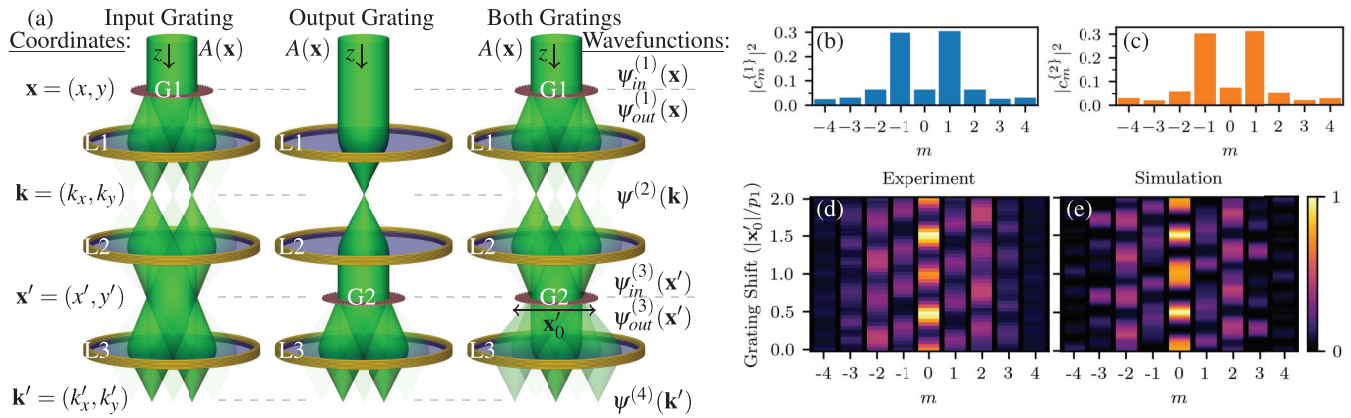


FIG. 1. (a) Diagram for 2GeMZI showing definitions of the different transverse planes as well as labels for the transverse wave functions in each plane, the magnetic lenses (L1, L2, L3), gratings (G1, G2), and beam-defining aperture $A(\mathbf{x})$ are also shown. The three different images depict the three cases of when the different gratings are inserted or removed. The position of the second grating relative to the beam is denoted as \mathbf{x}'_0 . (b) Diffraction efficiencies of G1, measured when G2 is removed. (c) Diffraction efficiencies of G2, measured when G1 is removed. (d) Measured output intensities of the 2GeMZI for different relative grating shifts normalized to maximum output intensity. (e) Simulated output intensities of the 2GeMZI for different relative grating shifts.

while retaining the precise interferometer alignments. To demonstrate the phase sensitivity of the 2GeMZI we map electrostatic potential differences in the vicinity of both grounded and charged silver nanorods and demonstrate quantitative nanoscale phase imaging of a spherical latex nanoparticle.

II. THEORETICAL DESCRIPTION OF ELECTRON INTERFEROMETER

In this electron interferometer, nanoscale diffraction gratings are used as amplitude-dividing beamsplitters and the standard TEM imaging optics are used to separate, scan, and recombine the beams. An illustration of this system can be seen in Fig. 1(a) where successive transverse planes are defined in relation to the previous plane by Fourier transform. The first beamsplitter in the interferometer is a grating (G1) in the x plane. The electron beam then passes through a lens (L1) that focuses and projects path path separated probes at the specimen, the k plane. The second lens (L2) projects an image of G1 onto the second grating (G2) in the \mathbf{x}' plane. Finally, the third lens (L3) projects the discrete outputs of the interferometer into the \mathbf{k}' plane at the detectors. Here we describe how the evolution of the electron wave function can be modeled throughout the interferometer.

The evolution of an electron wave function propagating through free space, neglecting spin, can be described by the Schrödinger equation with relativistic corrections. In a typical TEM with a field emission electron source, electrons are accelerated to beam energies of 40 to 300 keV with a 500 meV energy spread and the electron beam has very small beam divergence [38]. The evolution of electron wave functions can therefore be modeled using Fresnel and Fourier optical theory [39], consistent with the Schrodinger equation while assuming the electrons are largely quasimonochromatic, noninteracting, and collimated.

An electron wave function passing near or transmitting through an object can accumulate phase shifts and amplitude losses. In the weak phase approximation [39], these effects are proportional to the longitudinal extent of the interaction,

e.g., the thickness of the material. This can be described by a complex index of refraction $\eta = \sigma V_{\text{mip}} + i\gamma$, where $\sigma = 2\pi me\lambda/h^2$ is the object-independent interaction parameter for a free electron with relativistic mass m and de Broglie wavelength λ , V_{mip} is the mean inner potential of the material, and γ is a material-dependent decay coefficient that models coherent amplitude loss due to high-angle scattering. We use this complex index of refraction model to describe both the diffraction holograms we employ as beamsplitters and the specimens we image.

The transverse electron wave function incident on the input grating of the interferometer is assumed to be a plane wave with an outer edge defined by an aperture $\psi_{\text{in}}^{(1)}(\mathbf{x}) = A(\mathbf{x})$. When transmitted through a grating the wave function is modified by its transmission function

$$\psi_{\text{out}}^{(1)}(\mathbf{x}) = A(\mathbf{x})e^{i\eta t_1(\mathbf{x})}, \quad (1)$$

where $t_1(\mathbf{x})$ is the periodic thickness profile of the grating. For a straight grating with pitch p_1 and diffraction wavevector $\mathbf{k}_1 = 2\pi/p_1$, we can expand Eq. (1) by the Fourier series representation of the exponential term

$$\psi_{\text{out}}^{(1)}(\mathbf{x}) = A(\mathbf{x}) \sum_n c_n^{(1)} e^{in\mathbf{k}_1 \cdot \mathbf{x}}, \quad (2)$$

where the Fourier coefficients are given by

$$c_n^{(1)} = \frac{1}{p_1} \int_0^{p_1} d\tilde{x} e^{i\eta t_1(\tilde{x}) - in|\mathbf{k}_1| \tilde{x}} \quad (3)$$

where \tilde{x} is the 1d direction of the grating pitch. The unnormalized probes in the far-field after G1, focused in the back focal plane of the L1, can be expressed as

$$\psi^{(2)}(\mathbf{k}) \propto \sum_n c_n^{(1)} \tilde{A}(\mathbf{k} - n\mathbf{k}_1), \quad (4)$$

where \tilde{A} is the Fourier transformed A . Upon propagation to the \mathbf{x}' plane the wave function $\psi_{\text{in}}^{(3)}$ is exactly an image of $\psi_{\text{out}}^{(1)}$. If G2 is allowed to translate by an amount \mathbf{x}'_0 , then the output of

the second grating is

$$\psi_{\text{out}}^{(3)}(\mathbf{x}') \propto A(\mathbf{x}') \sum_{n,n'} c_n^{(1)*} c_{n'}^{(2)} e^{i\mathbf{n}'\mathbf{k}_2 \cdot (\mathbf{x}' - \mathbf{x}'_0) - i\mathbf{n}\mathbf{k}_1 \cdot \mathbf{x}'}, \quad (5)$$

where $c_n^{(2)}$ and \mathbf{k}_2 are similarly defined for the second grating. When the image of the input grating is projected onto the output grating with the same pitch and orientation, i.e., $\mathbf{k}_0 = \mathbf{k}_1 = \mathbf{k}_2$, the wave function in final \mathbf{k}' plane can be written as

$$\psi^{(4)}(\mathbf{k}') \propto \sum_{n,n'} c_n^{(1)*} c_{n'}^{(2)} e^{-i\mathbf{n}'\mathbf{k}_0 \cdot \mathbf{x}'_0} \tilde{A}(\mathbf{k}' - (n - n')\mathbf{k}_0). \quad (6)$$

The output of the interferometer is divided into distinct $m = n - n'$ diffraction orders. Using this to reindex the double sum, we can write Eq. (6) as a sum of output diffraction orders

$$\begin{aligned} \psi^{(4)}(\mathbf{k}') &\propto \sum_m \left(\sum_n c_n^{(1)*} c_{n-m}^{(2)} e^{-i(n-m)\mathbf{k}_0 \cdot \mathbf{x}'_0} \tilde{A}(\mathbf{k}' - m\mathbf{k}_0) \right) \\ &= \sum_m \psi_m^{(4)}(\mathbf{k}'). \end{aligned} \quad (7)$$

When the gratings are symmetric and put a majority of the transmitted intensity into the ± 1 st diffraction orders, i.e., $|c_{\pm 1}| \gg |c_{|m| \neq 1}|$ and $|c_{+1}| = |c_{-1}|$, then the 0th output diffraction order where $n = n'$, up to a global phase, is

$$\psi_0^{(4)}(\mathbf{k}') \propto |c_1^{(1)} c_1^{(2)}| (1 + e^{-2i\mathbf{k}_0 \cdot \mathbf{x}'_0}) \tilde{A}(\mathbf{k}') + \dots \quad (8)$$

If the probes are allowed to scan in the specimen plane, $\mathbf{k} \rightarrow \mathbf{k} + \mathbf{k}_s$, while passing through some electrostatic potential $V(\mathbf{k}, z)$, we can use the weak phase approximation and write the phase accumulated by each probe as being proportional to the projected potential along the z direction $\Phi(\mathbf{k}) = \sigma \int dz V(\mathbf{k}, z)$. Incorporating the phase due to a potential, the 0th order output of the interferometer is approximately

$$\psi_0^{(4)}(\mathbf{k}') \propto (1 + e^{i\varphi(\mathbf{k}_s, \mathbf{x}'_0)}) \tilde{A}(\mathbf{k}'), \quad (9)$$

where the total phase difference between the two highest intensity probes is

$$\varphi(\mathbf{k}_s, \mathbf{x}'_0) = -2\mathbf{k}_0 \cdot \mathbf{x}'_0 + \Phi(\mathbf{k}_s - \mathbf{k}_0) - \Phi(\mathbf{k}_s + \mathbf{k}_0). \quad (10)$$

We should note that the static potential V can have contributions that extend into the vacuum region due to the build up of surface charge on a material as well as inside materials from the mean inner potential as was defined in η .

III. CONSTRUCTION OF INTERFEROMETER

Two arrays of 350 nm pitch, 30 μm diameter binary phase gratings were each nanofabricated onto a $250 \times 250 \mu\text{m}^2$, 30-nm-thick, free-standing Si_3N_4 membrane using focused ion beam (FIB) gas-assisted etching [40]. To aid with alignment, the gratings were patterned at multiple orientations in a 6×6 array. In an image-corrected 80–300 keV FEI Titan TEM, one grating array was installed in the second condenser aperture and used as the first grating G1. The second grating array was installed in the post-specimen selected area aperture as the beam-combining grating G2. Both of these grating apertures

only take one of many aperture slots, so their installation does not impede the conventional functionalities of the TEM. The TEM was operated at 80 keV in STEM mode with approximately a 1 mrad convergence angle. An independently positionable circular aperture at the third condenser lens was used to select the output of a single grating out of the widely illuminated array of gratings. The diffraction orders created by the selected input grating were focused to narrow probes at the sample, the \mathbf{k} plane. The lenses were used in free lens control with assistance of the ‘‘Lorentz’’ lens in the image corrector to form a correctly magnified, oriented, and in-focus image of G1 onto G2. Finally, the post-G2 projection lenses were used to image the far-field diffraction pattern from both beamsplitters onto the detectors at the bottom of the TEM column. The relative grating shift parameter \mathbf{x}'_0 was controlled by the diffraction alignment coils in the image corrector that shifted the image of G1 relative to G2 allowing for arbitrary relative phase shifts between the two specimen plane probes in the interferometer output. The \mathbf{k} plane probes at the specimen section could be set to have up to 1 μm separation between the ± 1 probes, however the spot size increases proportionally with the probe separation. Using these beamsplitter gratings, the ratio between separation between the paths and the width of the probes is approximately 20.

The magnitude of the $\{c_n^{(1)}\}$ and $\{c_n^{(2)}\}$ Fourier coefficients were measured by inserting only one of G1 or G2 at a time while collecting an image of the probe intensities with a scintillator fiber-coupled CCD. A single diffraction order was integrated and divided by the total integrated intensity to determine normalized diffraction efficiencies $|c_n^{(1)}|^2$ and $|c_n^{(2)}|^2$; the measured grating outputs are shown in Figs. 1(b) and 1(c). Ideally, the gratings would be perfect binary gratings with 50% groove duty cycle with up to 40.5% of the transmitted intensity going into the ± 1 probes. However, edge rounding and nonideal duty cycles from nanofabrication with a finite width ion beam as well as over and under milling from the ideal groove depth caused deviations from the optimal diffraction efficiency. Even so, we were able to achieve dominant ± 1 coefficients allowing for efficient two-beam scanning in the 2GeMZI.

With G1 and G2 both inserted, we collected CCD images of the output beams for different values of \mathbf{x}'_0 by tuning the previously mentioned diffraction alignment coils. The measured output intensities are in good agreement with the expected result, Figs. 1(d) and 1(e). Without the presence of an electrostatic potential, the intensity of the 0th order interferometer output is expected to be proportional to the modulus square of Eq. (9), i.e., sinusoidal in the argument $\mathbf{k}_0 \cdot \mathbf{x}'_0$. We see this dependence in the experimental data, but it is also accompanied by a beating at half the spatial frequency $\mathbf{k}_0/2$. This amplitude beating is caused by a combination of grating duty cycle mismatch and contributions of the higher order terms from the sum of probe coefficients and is confirmed in the simulations that use simulated grating groove profiles that produce the experimentally measured far-field diffraction patterns in Figs. 1(b) and 1(c). Due to these higher order effects, the fringe visibility $\mathcal{V} = (I_{\text{max}} - I_{\text{min}})/(I_{\text{max}} + I_{\text{min}})$ is $\mathcal{V} = 0.76$ when the output is aligned for maximally destructive interference and $\mathcal{V} = 0.82$ when aligned for maximally constructive interference. The maximum theoretical fringe

visibility $\mathcal{V} = 1$ can be approached through the continued improvement of gratings.

Scan and descans coils can be used to raster both beams across a scan region up to three times the probe separation while keeping the electron interference pattern (the image of G1) stationary on G2, ensuring the interferometer output was constant while beams were scanned across a flat phase region. The scan/descan system is independent of the diffraction alignment used to control \mathbf{x}'_0 , so the relative phases between the interferometer probes remains constant throughout the scan. While scanning, a bright field (BF) monolithic detector can be inserted such that it is illuminated by only the 0th interferometer output order. With this configuration we can perform direct phase imaging with the 2GeMZI. The relative phase between the probes at any scan position in the specimen plane \mathbf{k}_s can be reconstructed from the intensity of the interferometer output

$$I_0^{(4)}(\mathbf{k}_s, \mathbf{x}'_0) \approx \langle I_0^{(4)} \rangle [1 + \mathcal{V} \cos(\varphi(\mathbf{k}_s, \mathbf{x}'_0))]. \quad (11)$$

It should be noted that phase shifts due to path length differences during the scan certainly exist, but are much smaller than the longitudinal coherence length, which for 80 keV electrons with a 500 meV energy spread is on the order of a micron. Throughout a scan, the scan/descan coils maintain the path length difference within a fraction of the electron's wavelength, as can be seen in flat intensity of the large vacuum scan region of Fig. 2(a), and so we can safely neglect this contribution to the relative probe phase.

IV. ELECTROSTATIC POTENTIALS IN THE INTERFEROMETER

One application of the 2GeMZI is mapping electrostatic potentials in real-time. In the last 30 years, quantitative potential maps measured with electron holography have been used to accurately determine charge distributions of nanoscale devices [41,42]. However streamlined this method has become, it still requires image post-processing or proprietary live analysis software [43,44]. While the high spatial and phase resolution of electron holography cannot yet be matched by the 2GeMZI in this initial demonstration, the interferometer provides a live interpretation of the electrostatic potential, whereas electron holography requires post-scan image processing. Each pixel's intensity indicates the electrostatic potential difference at the two probe positions in the specimen plane. Here we use the 2GeMZI to show the fringes in raw interferometric BF images of a grounded and insulated vertical nanorod.

We fabricated two 550-nm-tall vertical silver nanorods surrounded by a vacuum window; one with a conductive lead to ground and the other electrically insulated such that it would support a surface charge throughout an imaging scan (see Appendix for the sample fabrication details). This device was inserted in the specimen plane of the 2GeMZI which was adjusted to have a larger path separation of 500 nm with a probe size of about 25 nm. We recorded interferometric BF images over a scan region of $1.5 \times 1.5 \mu\text{m}^2$ of the grounded and insulated nanorods shown in Figs. 2(a) and 2(b). The electric potential from the semiconductor nitride substrate cantilever and the grounded nanorod was small; as shown in Fig. 2(a),

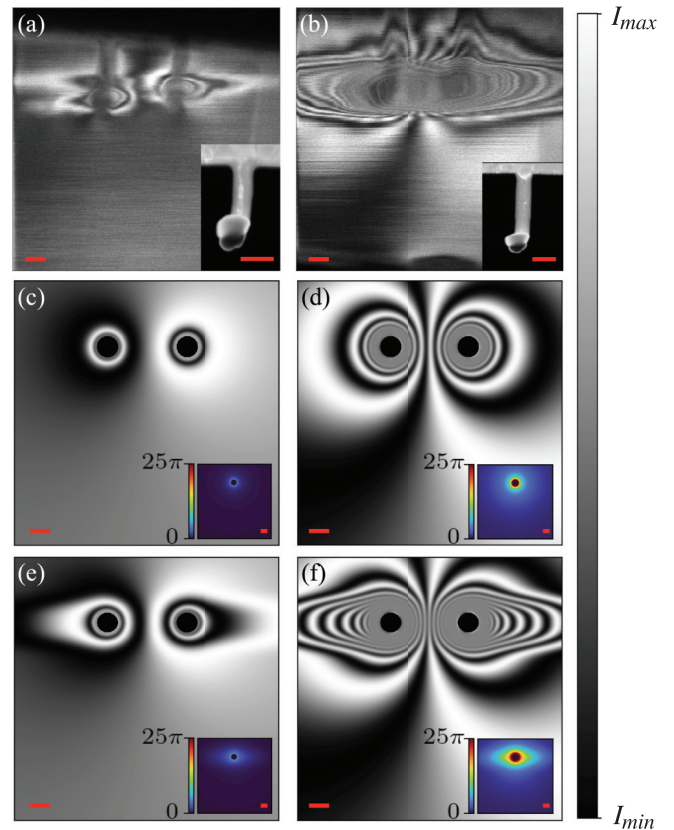


FIG. 2. Bright field (BF) STEM images showing the interferometer output spatially oscillating between the intensity minimum and maximum for (a) grounded vertical Ag nanorod, (b) insulated vertical Ag nanorod. Insets are STEM HAADF images of each nanorod. [(c) and (d)] Simulated 2GeMZI output for two probes passing through a $1/r$ electrostatic potential where (d) has 10 times the charge of (c). [(e) and (f)] Same as (c) and (d) but with a horizontally elongated Gaussian included with the potential to simulate the increased induced charging by the incidence of the higher diffraction orders. Insets in (c)–(f) are the projected potentials used to create the simulated images. All scale bars are 100 nm.

the interferometer output was only modulated close to the surface of the nitride and the relative phase between two probes in the vacuum region far away from the object is constant. However, the electrically insulated nanorod charged when exposed to the beam until reaching a static surface charge, creating a larger static potential. The resulting interference fringes for the probe potential differences can clearly be seen far into the surrounding vacuum region, as shown in Fig. 2(b). Close to the nanorod, the larger gradient in electrostatic potential induces a phase that varies within the width of the probes, resulting in a loss of fringe visibility.

We use a $1/r$ potential to approximate the nonlinear monotonically decreasing behavior that is expected surrounding a charged vertical nanorod [Figs. 2(c) and 2(d)]. In the experimental interferometric BF images, there is elongation in the probe separation direction that is not shown in this simple model, but this can be explained by an increased surface charge on the nanorod when the higher order probes ($m \neq \pm 1$) are incident on the specimen. Including a Gaussian background to the $1/r$ potential elongated in the probe separation

direction to account for this increase in surface charge creates an interference pattern that is qualitatively consistent with the experimental images [Figs. 2(e) and 2(f)].

This initial demonstration shows that the 2GeMZI is sensitive to differences in electrostatic potentials at the locations of the two probes: spatially varying electrostatic potentials impart a phase to the specimen probes and the phase difference modulates the intensity at the BF detector. With moderate improvements, the real-time interferometric BF images can provide nanoscale maps of the static projected potential with higher phase resolution. Some challenges still need to be overcome to achieve quantitative real-time potential mapping, especially for determining static charge distributions. First, is to ensure the static charge is independent of the scanning probes which can be accomplished with adequately grounded, conductive materials. Second, is to limit the samples of interest such that the spatial extent of the potential does not extend over multiple probes. This ensures there is a reference probe and a measurement probe with a phase difference that is directly proportional to the projected potential. This second point can be relaxed with a careful analysis and full understanding of the accumulated relative phases between all the probes as they are scanned into the potential. Third, smaller probe sizes must be used to probe potentials with large spatial gradients.

V. QUANTITATIVE PHASE IMAGING OF A LATEX NANOPARTICLE

To demonstrate an example of quantitative phase imaging with the 2GeMZI, we imaged polystyrene latex spherical nanoparticles on a suspended single layer of graphene. Polystyrene latex has a well-characterized mean inner potential, $V_{\text{mip}}^{\text{latex}} = 8.5 \pm 0.7 \text{ V}$ [45], and small amplitude decay coefficient, $\gamma^{\text{latex}} \approx 0$. We use a nanosphere with a diameter of 60 nm. The ratio of probe size and separation is fixed, but can be simultaneously tuned by changing the lens magnification settings. Here the 2GeMZI was tuned for a probe separation of $92 \pm 2 \text{ nm}$ and a focused beam width of approximately 5 nm such that one of the two 2GeMZI probes could be scanned through the nanosphere while the other passed through uniform graphene in the specimen plane (Fig. 3). The phase imparted by the graphene is expected to be about 45 mrad [46]. Individual atoms are not resolvable at the resolution in this initial demonstration, so we treat the sample as a homogeneous latex sphere with a small uniform phase background. Another benefit of the graphene substrate is that it efficiently alleviates charge, allowing us to disregard extraneous static fields due to sample charging and only consider the mean inner potential from the latex as the source of the probe phase shift. Due to the size of the nanoparticle in comparison to the large probe separation, the elimination of electrostatic fields, and the negligible decay coefficient of latex, we can assume the phase difference between the two probes is

$$\varphi(\mathbf{k}_s, \mathbf{x}'_0) = -2\mathbf{k}_0 \cdot \mathbf{x}'_0 + \sigma V_{\text{mip}}^{\text{latex}} t_{\text{sph}}(\mathbf{k}_s). \quad (12)$$

The first term, $2\mathbf{k}_0 \cdot \mathbf{x}'_0$, is due to the interferometer alignment and the last, $\sigma V_{\text{mip}}^{\text{latex}} t_{\text{sph}}(\mathbf{k}_s)$, is the phase accumulated by the probe passing through the sphere of projected thick-

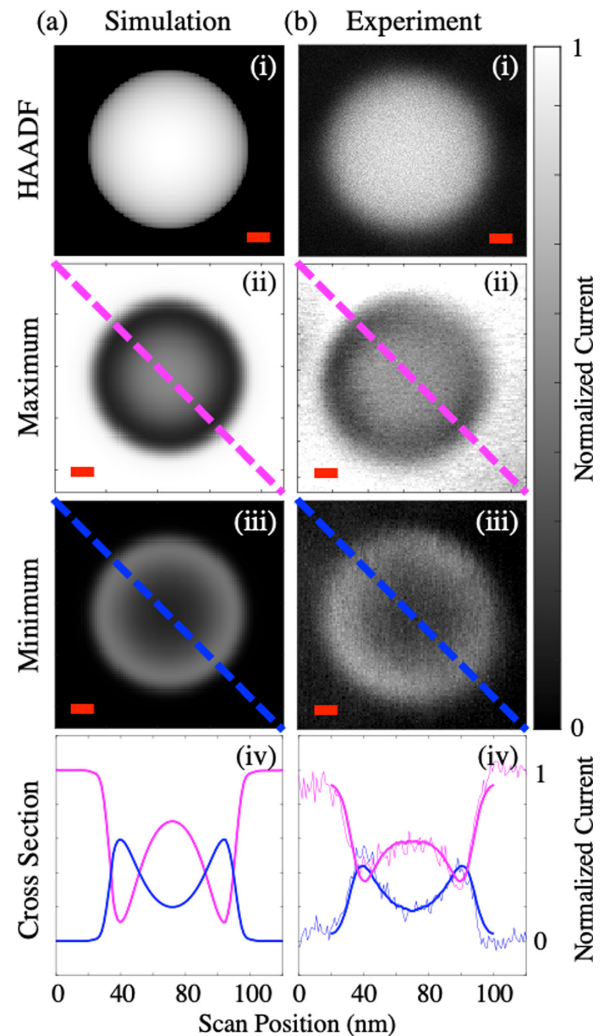


FIG. 3. HAADF and 2GeMZI BF image scans of a latex nanoparticle both from (a) simulation and (b) experiment. The rows display (i) the HAADF image, the 2GeMZI image aligned at the maximally (ii) constructive (magenta) and (iii) destructive (blue) interferometer output, and (iv) the respective line profiles. The experimental cross section [b(iv)] shows a raw cross section (thin line) and the radially averaged signal (thick line). All scale bars are 10 nm.

ness $t_{\text{sph}}(\mathbf{k}_s)$ at the scan location \mathbf{k}_s . The latex spheres were interferometrically imaged by scanning the probes over a $100 \times 100 \text{ nm}^2$ scan region while the 0th order interferometer output was recorded by the BF detector.

We recovered the phase image of the 60 nm diameter latex nanoparticle from two interferometric BF images, one with the interferometer initially aligned for maximally constructive 0th order output, $2\mathbf{k}_0 \cdot \mathbf{x}'_0 = \pi$ [Fig. 3(ii)] and one aligned for destructive output $2\mathbf{k}_0 \cdot \mathbf{x}'_0 = 0$ [Fig. 3(iii)]. To map each pixel's intensity onto a phase, we first find the center of the nanoparticle and take an azimuthal average of the intensity to exploit the particle's symmetry. This provides an intensity line profile across the nanoparticle and graphene from the constructive and destructive interferometric images [Fig. 3(iv)]. Exploiting the phase continuity of the spherical nanoparticle, we note that the phase should be monotonically increasing from the graphene substrate to the center of the nanoparticle. We set the phase of the graphene substrate to zero, as a

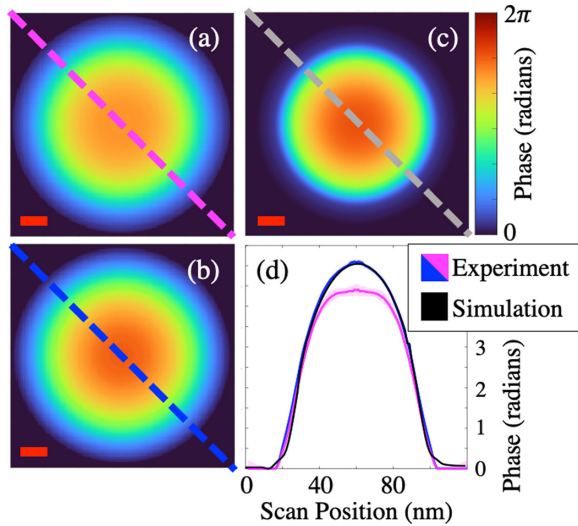


FIG. 4. Reconstructed azimuthally averaged phase images of a latex nanoparticle from the raw 2GeMZI BF images with (a) constructive alignment (magenta) and (b) destructive alignment (blue). The simulated outcome (c) is also shown. (d) The experimental and simulated cross-sections of the reconstructed particle phase with shaded regions to show the error. All scale bars are 10 nm.

reference. Using the co-sinusoidal relation between phase and intensity found in Eq. (11), we map the intensity profile to a phase profile. From these radial phase profiles, we reconstruct a phase image of the particle, as shown in Fig. 4.

Using the experimental Fourier coefficients which define each grating, a 5 nm spot size, 100 nm probe separation and assuming the nanoparticle is a perfectly spherical phase object, we simulate the expected intensity output in the BF detector when the positive first order probe interacts with the sample for both alignment schemes [Fig. 3(a)]. The simulated intensity profile is then mapped to phase using the same mechanism as described above. The experimental phase profiles undershoot the simulated results [Fig. 4(d)] because the nanoparticle’s amplitude decay coefficient is not exactly zero. The discrepancy between the constructively and destructively interfering experimental results can also be attributed to the amplitude decay. Decoupling the amplitude loss and imparted phase is a subject of ongoing work. The experimental phase profile of the nanosphere is slightly wider than the simulated results, due to the large probe size and the induced charging effects.

VI. DISCUSSION

The 2GeMZI achieves qualitative real-time phase imaging and quantitative phase recovery providing a platform for low-dose imaging, interaction-free measurements, subnanometer live phase imaging, and experiments probing the Aharonov-Bohm effect.

A phase resolution of $\sigma_{\text{ph}} = 240$ mrad has been achieved; the phase precision could be improved with enhanced gratings, a smaller probe size, longer exposure times with efficient charge alleviation, or a lower noise BF detector. Another benefit of an improved detector is that the 512×512 pixel image, 1 Hz frame rate of this initial demonstration can be significantly increased. At the single electron detection

level, with improved grating efficiency [40], and a high frame rate, unambiguous interaction-free imaging could be realized; these improvements have already been shown individually, so incorporation into the 2GeMZI is not an insurmountable task and would significantly improve our previous demonstration of interaction-free measurements with electrons [5].

Considering grating-based STEM holography achieved 30 mrad phase and subnanometer spatial resolutions [47], there is promise for atomic resolution phase imaging with this technique, but in real-time without image post processing. The spatial resolution of the 2GeMZI is limited by the focused probe width, which is tunable by selecting different convergence angles using the lens system. Subnanometer resolution can be achieved in our device with a smaller grating pitch and larger aperture diameter. The limiting factor in this case is the stability of the scan/descan coils in the microscope keeping the image of G1 on G2 stationary to within a small fraction of the grating pitch throughout an imaging scan, making it difficult to reach a sufficient probe separation with subnanometer probes. The 1 μm that was demonstrated here could be safely improved by up to a factor of 2 without a loss of efficiency by decreasing the grating pitch.

It has been shown that the path separation between the probes from a grating interferometer can be increased by more than order of magnitude by the inclusion of biprisms in intermediate planes, between the \mathbf{x} and \mathbf{k} planes [48]. Although this would require a highly specialized microscope, such large path separations would allow for a more isolated reference beam for phase imaging and could more readily enable fundamental experiments such as testing the limits of the Aharonov-Bohm effect [49] and decoherence theory [10].

VII. CONCLUSION

We constructed a scanning, path-separated, two-grating Mach-Zehnder interferometer for free electrons by employing two nanofabricated diffraction grating holograms in a conventional TEM. Although each figure of merit can be tuned or improved, the initial implementation shown here has an interference contrast of 82%, a path separation of up to 1 μm , a demonstrated phase resolution of approximately $\sigma_{\text{ph}} = 240$ mrad, and an output current on the order of tens of picoamps. We qualitatively showed that the 2GeMZI is sensitive to phase shifts due to electrostatic potentials in vacuum by imaging the potential differences around both grounded and insulated silver vertical nanorods. We then quantitatively recovered the phase of a polystyrene latex nanoparticle on graphene. The 2GeMZI is particularly impactful in free electron interferometry due to its tunable probe separation, the accessibility of individual paths, the ability to arbitrarily apply phase shifts between separate paths, its scanning capabilities, and the real-time phase information at the nanoscale.

With incremental improvements in grating beamsplitters and detectors, the 2GeMZI could be used for interaction-free electron imaging [6,7], low-dose STEM imaging [50,51], nanoscale magnetic imaging [52], fundamental quantum physics experiments such as the Aharonov-Bohm effect [4], and furthering decoherence theory [53,54]. Subjects of ongoing work are decoupling the imparted phase and amplitude loss, enhancing the contrast at the detector, and improving

the spatial and phase resolution. Due to the flexible design and broad applications, the 2GeMZI is uniquely positioned in electron microscopy to open doors to subnanometer electron interferometry and low-dose, high-resolution microscopy.

ACKNOWLEDGMENTS

We thank Joshua Razink and Valerie Brogden for TEM and SEM/FIB instrument support. This material is based upon work supported by the National Science Foundation under Grants No. 1607733 and No. 2012191. C.W.J. was supported by the NSF GRFP Grant No. 1309047.

APPENDIX: VERTICAL NANOROD FABRICATION

Using a Ga⁺ FIB operated at 30 keV with a 7.7-pA beam current, we fabricated vertical silver nanorods on a nitride cantilever from a 100-nm-thick silver film thermally deposited on a 50-nm-thick Si₃N₄ membrane in the following steps.

(i) Mill completely through silver and nitride forming cylindrical silver bead along nitride tether.

(ii) Mill only through silver defining bottom edge of nanorod, optionally leaving a small lead of silver between the rod and the film.

(iii) Mill completely through silver and nitride defining top edge of rod and nitride cantilever.

(iv) Flip membrane over and raster FIB over the bare nitride section of cantilever to induce bending until the nanorod is vertical, normal to the silver film and nitride membrane [55].

These nanorods were fabricated with a clear vacuum region around the rods for easy access for imaging in the 2GeMZI. One of the two nanorods was given a small lead to ground

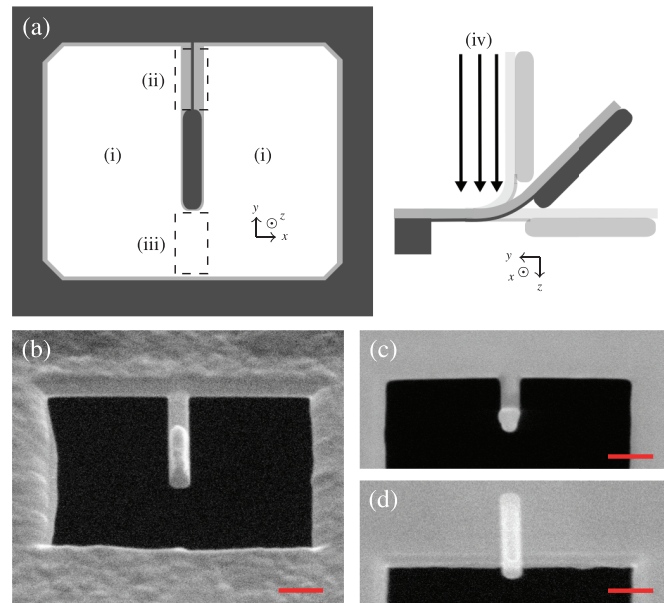


FIG. 5. (a) Vertical silver nanorod FIB nanofabrication steps (i)–(iv). (b) SEM micrograph at 52° tilt after fabrication steps (i)–(iii). SEM micrographs after fabrication steps (i)–(iv) imaging from bottom of membrane at (c) 0° and (d) 52° tilt. All scale bars are 200 nm.

to the rest of the silver film, while the other was electrically insulated by removing all of the silver between the nanorod and the film. An illustration of the fabrication process can be seen in Fig. 5(a) accompanied by scanning electron microscopy (SEM) micrographs displaying the sample geometry and orientation, Figs. 5(b)–5(d).

- [1] A. Tonomura, *Electron Holography*, 2nd ed., Springer Series in Optical Sciences (Springer-Verlag, Berlin Heidelberg, 1999).
- [2] R. E. Dunin-Borkowski, A. Kovács, T. Kasama, M. R. McCartney, and D. J. Smith, *Electron Holography*, in *Springer Handbook of Microscopy*, edited by P. W. Hawkes and J. C. H. Spence, Springer Handbooks (Springer International, Cham, 2019), pp. 767–818.
- [3] A. Tonomura, N. Osakabe, T. Matsuda, T. Kawasaki, J. Endo, S. Yano, and H. Yamada, Evidence for Aharonov-Bohm Effect with Magnetic Field Completely Shielded from Electron Wave, *Phys. Rev. Lett.* **56**, 792 (1986).
- [4] H. Batelaan and A. Tonomura, The Aharonov-Bohm effects: Variations on a subtle theme, *Phys. Today* **62**(9), 38 (2009).
- [5] A. E. Turner, C. W. Johnson, P. Kruit, and B. J. McMoran, Interaction-Free Measurement with Electrons, *Phys. Rev. Lett.* **127**, 110401 (2021).
- [6] W. P. Putnam and M. F. Yanik, Noninvasive electron microscopy with interaction-free quantum measurements, *Phys. Rev. A* **80**, 040902(R) (2009).
- [7] P. Kruit, R. Hobbs, C.-S. Kim, Y. Yang, V. Manfrinato, J. Hammer, S. Thomas, P. Weber, B. Klopfer, C. Kohstall, T. Juffmann, M. Kasevich, P. Hommelhoff, and K. Berggren, Designs for a quantum electron microscope, *Ultramicroscopy* **164**, 31 (2016).
- [8] P. L. Potapov, J. Verbeeck, P. Schattschneider, H. Lichte, and D. van Dyck, Inelastic electron holography as a variant of the Feynman thought experiment, *Ultramicroscopy* **107**, 559 (2007).
- [9] A. Pooch, M. Seidling, N. Kerker, R. Röpke, A. Rembold, W. T. Chang, I. S. Hwang, and A. Stibor, Coherent properties of a tunable low-energy electron-matter-wave source, *Phys. Rev. A* **97**, 013611 (2018).
- [10] N. Kerker, R. Röpke, L. M. Steinert, A. Pooch, and A. Stibor, Quantum decoherence by Coulomb interaction, *New J. Phys.* **22**, 063039 (2020).
- [11] K. E. Priebe, C. Rathje, S. V. Yalunin, T. Hohage, A. Feist, S. Schäfer, and C. Ropers, Attosecond electron pulse trains and quantum state reconstruction in ultrafast transmission electron microscopy, *Nat. Photonics* **11**, 793 (2017).
- [12] I. Madan, G. M. Vanacore, E. Pomarico, G. Berruto, R. J. Lamb, D. McGrouther, T. T. A. Lummen, T. Latychevskaia, F. J. G. d. Abajo, and F. Carbone, Holographic imaging of electromagnetic fields via electron-light quantum interference, *Sci. Adv.* **5**, eaav8358 (2019).

- [13] K. E. Echternkamp, A. Feist, S. Schäfer, and C. Ropers, Ramsey-type phase control of free-electron beams, *Nat. Phys.* **12**, 1000 (2016).
- [14] J. D. Monnier, Optical interferometry in astronomy, *Rep. Prog. Phys.* **66**, 789 (2003).
- [15] P. J. de Groot, A review of selected topics in interferometric optical metrology, *Rep. Prog. Phys.* **82**, 056101 (2019).
- [16] J.-W. Pan, Z.-B. Chen, C.-Y. Lu, H. Weinfurter, A. Zeilinger, and M. Żukowski, Multiphoton entanglement and interferometry, *Rev. Mod. Phys.* **84**, 777 (2012).
- [17] M. A. R. Krielaart and P. Kruit, Grating mirror for diffraction of electrons, *Phys. Rev. A* **98**, 063806 (2018).
- [18] N. Abedzadeh, M. A. R. Krielaart, C.-S. Kim, J. Simonaitis, R. Hobbs, P. Kruit, and K. K. Berggren, Electrostatic electron mirror in SEM for simultaneous imaging of top and bottom surfaces of a sample, [arXiv:2012.09902](https://arxiv.org/abs/2012.09902) [physics].
- [19] M. A. R. Krielaart and P. Kruit, Flat electron mirror, *Ultramicroscopy* **220**, 113157 (2021).
- [20] H. Lichte, P. Formanek, A. Lenk, M. Linck, C. Matzeck, M. Lehmann, and P. Simon, Electron holography: Applications to materials questions, *Annu. Rev. Mater. Res.* **37**, 539 (2007).
- [21] S. L. Y. Chang, C. Dwyer, C. B. Boothroyd, and R. E. Dunin-Borkowski, Optimising electron holography in the presence of partial coherence and instrument instabilities, *Ultramicroscopy* **151**, 37 (2015).
- [22] R. Harvey, J. S. Pierce, A. K. Agrawal, P. Ercius, M. Linck, and B. J. McMorran, Efficient diffractive phase optics for electrons, *New J. Phys.* **16**, 093039 (2014).
- [23] D. L. Freimund, K. Aflatooni, and H. Batelaan, Observation of the Kapitza-Dirac effect, *Nature (London)* **413**, 142 (2001).
- [24] A. Feist, S. V. Yalunin, S. Schäfer, and C. Ropers, High-purity free-electron momentum states prepared by three-dimensional optical phase modulation, *Phys. Rev. Res.* **2**, 043227 (2020).
- [25] F. S. Yasin, T. R. Harvey, J. J. Chess, J. S. Pierce, and B. J. McMorran, Path-separated electron interferometry in a scanning transmission electron microscope, *J. Phys. D: Appl. Phys.* **51**, 205104 (2018).
- [26] R. Zimmermann, P. Weber, M. Seidling, and P. Hommelhoff, Beam splitting of low-energy guided electrons with a two-sided microwave chip, *Appl. Phys. Lett.* **115**, 104103 (2019).
- [27] L. Marton, Electron Interferometer, *Phys. Rev.* **85**, 1057 (1952).
- [28] H. Rauch and S. A. Werner, *Neutron Interferometry: Lessons in Experimental Quantum Mechanics, Wave-Particle Duality, and Entanglement* (Oxford University Press, 2015).
- [29] A. D. Cronin, J. Schmiedmayer, and D. E. Pritchard, Optics and interferometry with atoms and molecules, *Rev. Mod. Phys.* **81**, 1051 (2009).
- [30] T. Berrada, S. van Frank, R. Bücke, T. Schumm, J.-F. Schaff, and J. Schmiedmayer, Integrated Mach-Zehnder interferometer for Bose-Einstein condensates, *Nat. Commun.* **4**, 2077 (2013).
- [31] Y. Ji, Y. Chung, D. Sprinzak, M. Heiblum, D. Mahalu, and H. Shtrikman, An electronic Mach-Zehnder interferometer, *Nature (London)* **422**, 415 (2003).
- [32] M. Jo, P. Brasseur, A. Assouline, G. Fleury, H.-S. Sim, K. Watanabe, T. Taniguchi, W. Dumernpanich, P. Roche, D. C. Glatli, N. Kumada, F. D. Parmentier, and P. Roulleau, Quantum Hall Valley Splitters and a Tunable Mach-Zehnder Interferometer in Graphene, *Phys. Rev. Lett.* **126**, 146803 (2021).
- [33] W. D. Oliver, Y. Yu, J. C. Lee, K. K. Berggren, L. S. Levitov, and T. P. Orlando, Mach-Zehnder interferometry in a strongly driven superconducting qubit, *Science* **310**, 1653 (2005).
- [34] A. H. Tavabi, M. Duchamp, V. Grillo, R. E. Dunin-Borkowski, and G. Pozzi, New experiments with a double crystal electron interferometer, *Eur. Phys. J. Appl. Phys.* **78**, 10701 (2017).
- [35] A. Agarwal, C.-S. Kim, R. Hobbs, D. v. Dyck, and K. K. Berggren, A nanofabricated, monolithic, path-separated electron interferometer, *Sci. Rep.* **7**, 1677 (2017).
- [36] L. Marton, J. A. Simpson, and J. A. Suddeth, An electron interferometer, *Rev. Sci. Instrum.* **25**, 1099 (1954).
- [37] G. Gronniger, B. Barwick, and H. Batelaan, A three-grating electron interferometer, *New J. Phys.* **8**, 224 (2006).
- [38] L. Reimer, *Transmission Electron Microscopy: Physics of Image Formation and Microanalysis*, Springer Series in Optical Sciences (Springer, Berlin, Heidelberg, 2013).
- [39] J. M. Cowley and S. Iijima, Electron Microscope Image Contrast for Thin Crystal, *Z. Naturforsch. A* **27**, 445 (1972).
- [40] C. W. Johnson, D. H. Bauer, and B. J. McMorran, Improved control of electron computer-generated holographic grating groove profiles using ion beam gas-assisted etching, *Appl. Opt.* **59**, 1594 (2020).
- [41] G. Matteucci, G. F. Missiroli, M. Muccini, and G. Pozzi, Electron holography in the study of the electrostatic fields: The case of charged microtips, *Ultramicroscopy* **45**, 77 (1992).
- [42] V. Migunov, A. London, M. Farle, and R. E. Dunin-Borkowski, Model-independent measurement of the charge density distribution along an Fe atom probe needle using off-axis electron holography without mean inner potential effects, *J. Appl. Phys.* **117**, 134301 (2015).
- [43] M. R. McCartney and D. J. Smith, Electron holography: Phase imaging with nanometer resolution, *Annu. Rev. Mater. Res.* **37**, 729 (2007).
- [44] E. Voelkl, F. Zheng, V. Migunov, M. Beleggia, and R. E. Dunin-Borkowski, Live measurement of electrical charge density in materials using off-axis electron holography, *Microsc. Microanal.* **25**, 44 (2019).
- [45] Y. Wang, T. Chou, M. Libera, E. Voelkl, and B. Frost, Measurement of polystyrene mean inner potential by transmission electron holography of latex spheres, *Microsc. Microanal.* **4**, 146 (1998).
- [46] D. Cooper, C.-T. Pan, and S. Haigh, Atomic resolution electrostatic potential mapping of graphene sheets by off-axis electron holography, *J. Appl. Phys.* **115**, 233709 (2014).
- [47] F. S. Yasin, T. R. Harvey, J. J. Chess, J. S. Pierce, C. Ophus, P. Ercius, and B. J. McMorran, Probing Light atoms at subnanometer resolution: Realization of scanning transmission electron microscope holography, *Nano Lett.* **18**, 7118 (2018).
- [48] F. S. Yasin, K. Harada, D. Shindo, H. Shinada, B. J. McMorran, and T. Tanigaki, A tunable path-separated electron interferometer with an amplitude-dividing grating beamsplitter, *Appl. Phys. Lett.* **113**, 233102 (2018).
- [49] A. Caprez, B. Barwick, and H. Batelaan, Macroscopic Test of the Aharonov-Bohm Effect, *Phys. Rev. Lett.* **99**, 210401 (2007).
- [50] C. Ophus, J. Ciston, J. Pierce, T. R. Harvey, J. Chess, B. J. McMorran, C. Czarnik, H. H. Rose, and P. Ercius, Efficient linear phase contrast in scanning transmission electron microscopy

- with matched illumination and detector interferometry, *Nat. Commun.* **7**, 10719 (2016).
- [51] A. Agarwal, K. K. Berggren, Y. J. van Staaden, and V. K. Goyal, Reduced damage in electron microscopy by using interaction-free measurement and conditional reillumination, *Phys. Rev. A* **99**, 063809 (2019).
- [52] A. Greenberg, B. McMorran, C. Johnson, and F. Yasin, Magnetic phase imaging using interferometric STEM, *Microsc. Microanal.* **26**, 2480 (2020).
- [53] P. Schattschneider and S. Löffler, Entanglement and decoherence in electron microscopy, *Ultramicroscopy* **190**, 39 (2018).
- [54] P. J. Beierle, L. Zhang, and H. Batelaan, Experimental test of decoherence theory using electron matter waves, *New J. Phys.* **20**, 113030 (2018).
- [55] A. Cui, J. C. Fenton, W. Li, T. H. Shen, Z. Liu, Q. Luo, and C. Gu, Ion-beam-induced bending of freestanding amorphous nanowires: The importance of the substrate material and charging, *Appl. Phys. Lett.* **102**, 213112 (2013).